

Article

# Unexpected Ground-State Structure and Mechanical Properties of Ir<sub>2</sub>Zr Intermetallic Compound

Meiguang Zhang <sup>1,\*</sup>, Rui Cao <sup>1</sup>, Meijie Zhao <sup>1</sup>, Juan Du <sup>1</sup> and Ke Cheng <sup>2</sup>

<sup>1</sup> College of Physics and Optoelectronics Technology, Baoji University of Arts and Sciences, Baoji 721016, China; RuiCaobj@126.com (R.C.); MeijieZhao1@126.com (M.Z.); JuanDub@126.com (J.D.)

<sup>2</sup> College of Optoelectronic Technology, Chengdu University of Information Technology, Chengdu 610225, China; ck@cuit.edu.cn

\* Correspondence: yuan@ntou.edu.tw; Tel.: +86-917-336-4258

Received: 12 December 2017; Accepted: 9 January 2018; Published: 10 January 2018

**Abstract:** Using an unbiased structure searching method, a new orthorhombic *Cmmm* structure consisting of ZrIr<sub>12</sub> polyhedron building blocks is predicted to be the thermodynamic ground-state of stoichiometric intermetallic Ir<sub>2</sub>Zr in Ir-Zr systems. The formation enthalpy of the *Cmmm* structure is considerably lower than that of the previously synthesized Cu<sub>2</sub>Mg-type phase, by ~107 meV/atom, as demonstrated by the calculation of formation enthalpy. Meanwhile, the phonon dispersion calculations further confirmed the dynamical stability of *Cmmm* phase under ambient conditions. The mechanical properties, including elastic stability, rigidity, and incompressibility, as well as the elastic anisotropy of *Cmmm*-Ir<sub>2</sub>Zr intermetallic, have thus been fully determined. It is found that the predicted *Cmmm* phase exhibits nearly elastic isotropic and great resistance to shear deformations within the (100) crystal plane. Evidence of atomic bonding related to the structural stability for Ir<sub>2</sub>Zr were manifested by calculations of the electronic structures.

**Keywords:** first-principles calculations; ground-state structure; Ir<sub>2</sub>Zr intermetallic; mechanical properties

## 1. Introduction

The platinum-group metals (PGMs)—osmium, iridium, platinum, ruthenium, rhodium, and palladium—are immensely important in numerous technologies, but the experimental and computational data on their binary alloys still contain many gaps. In contrast to other transition metals [1–3], interest in PGMs is driven by their essential role in a wide variety of industrial applications, which is at odds with their high cost. The primary application of PGMs is in catalysis, where they are core ingredients in the chemical, petroleum, and automotive industries. Recently, the Ir-Zr binary alloys have become a topic that is currently attracting considerable interest for their potential applications in aeronautics and electronics applications. Like Ni-based alloys, Ir-Zr alloys have a two-phase face-centered cubic (*fcc*)/L1<sub>2</sub> structure, with the L1<sub>2</sub> (Ir<sub>3</sub>Zr) precipitates coherently embedded in the *fcc* Ir matrix, and such an alloy with *fcc*/L1<sub>2</sub> interfaces has been found to have higher strength than the single *fcc* or L1<sub>2</sub> intermetallic [4–8]. Moreover, it has been demonstrated that, for a given alloy, some unexpected stoichiometric intermetallics would appear in its microstructure during different heating and cooling processes, which would have a great effect on the properties of the alloys [9–11]. For instance, it has been reported that the phase transformation of IrZr significantly contributes to the great high-temperature shape memory effect for Ir-Zr alloys [10,11]. Hence, an insight into the intrinsic properties of the intermetallics, such as their mechanical properties, could be of great practical significance for the design of composite materials.

The Ir-Zr binary system has been reviewed by Okamoto [12], where the phase diagram was based primarily on the high-temperature X-ray and thermal analyses conducted by Eremenko et al. [13]. Six known stoichiometric intermetallics—Ir<sub>3</sub>Zr, Ir<sub>2</sub>Zr, IrZr, Ir<sub>3</sub>Zr<sub>5</sub>, IrZr<sub>2</sub>, and IrZr<sub>3</sub>—have

been determined, in which Ir<sub>3</sub>Zr and IrZr melted congruently, and the others were formed by peritectic or peritectoid reactions. The follow-up studies on their structures, mechanical, thermodynamic, and dislocation properties have evoked significant interest in their potential applications. It is known that crystal structures are the key for understanding the mechanical properties of materials [14–18]. Thus, the crystal structures of these six intermetallic compounds have been extensively studied. Except for IrZr and Ir<sub>2</sub>Zr, consensus has been reached that the intermetallic phases Ir<sub>3</sub>Zr, Ir<sub>3</sub>Zr<sub>5</sub>, IrZr<sub>2</sub>, and IrZr<sub>3</sub> adopt cubic Cu<sub>3</sub>Au-type (*Pm* $\bar{3}$ *m*, *Z* = 1), hexagonal Mn<sub>5</sub>Si<sub>3</sub>-type (*P*6<sub>3</sub>/*mcm*, *Z* = 2), tetragonal Al<sub>2</sub>Cu-type (*I*4/*mcm*, *Z* = 4), and tetragonal V<sub>3</sub>S-type (*I* $\bar{4}$ *m*2, *Z* = 8) structures, respectively. For IrZr, different room-temperature structures, including TiNi-type, FeB-type, and CrB-type, have been proposed, while a new orthorhombic *Cmcm* structure was experimentally characterized to be the most stable phase for IrZr [15], and was confirmed by the theoretical work in [10,16,18]. However, the crystal structure of Ir<sub>2</sub>Zr is the subject of continuing debate. Ir<sub>2</sub>Zr was proposed to have the C15 (Cu<sub>2</sub>Mg-type) structure [13], while recently, it was theoretically suggested to be unstable through formation enthalpy calculations [18]. Compared to IrZr, experimental and theoretical investigation of the crystal structures of Ir<sub>2</sub>Zr have rarely been undertaken, and there is a lack of confirmed reports on the existence of ground-state structure. Therefore, the peculiarity and the absence of characterized stable structures of Ir<sub>2</sub>Zr prompted our endeavor to investigate its structural stability under ambient conditions. Furthermore, the explorations of ground-state structures and related mechanical properties would provide more insights on other Ir-based intermetallic compounds. In order to address these points, we here performed extensive structure searches to explore the potential energetically stable Ir<sub>2</sub>Zr phase at ambient pressure using the newly developed Crystal structure AnaLYsis by Particle Swarm Optimization package (CALYPSO) [19,20], unbiased by any known information. This method has been successfully applied to extensive structures that have been confirmed by independent experiments [21–23]. Indeed, an orthorhombic *Cmmm* structure is uncovered to be the best ground-state candidate for Ir<sub>2</sub>Zr, and the crystal structures, mechanical behaviors, and electronic structures of this new phase were then fully investigated in comparison with the proposed Cu<sub>2</sub>Mg-type phase.

## 2. Computational Methods

The crystal structure searches for Ir<sub>2</sub>Zr were performed based on a global minimization of energy surfaces merging first-principle total-energy calculations as implemented in CALYPSO code [19,20], which was designed to predict stable or metastable crystal structures requiring only chemical compositions of a given compound at given external conditions (e.g., pressure). Here, using the CALYPSO code in combination with Vienna ab initio simulation package (VASP) [24], variable cell structure searches for Ir<sub>2</sub>Zr containing 1–6 formula units (f.u.) in the simulation cell were systematically performed at ambient pressure. During the structure searches, the 60% of the structures of each generation with the lowest enthalpies were selected to generate the structures for the next generation by Particle Swarm Optimization (PSO) operation, and the other structures in new generation were randomly generated to increase the structural diversity. The following local structural relaxations and electronic calculations were performed using the VASP code, in which the generalized-gradient approximation proposed by Perdew-Burke-Ernzerhof exchange-correlation functional [25,26] was used for the full optimization of all crystal structures. The electron and core interactions were included by using the frozen-core all-electron projector augmented wave potential of the metal atoms including d electrons as valence states [27]. The cutoff energy of 600 eV for the plane-wave expansions and dense *k*-point with grid density of  $0.03 \times 2\pi \text{ \AA}^{-1}$  (Monkhorst-Pack scheme) [28] were used in the Brillouin zone integration. The total energy and stress calculations were performed by using the tetrahedron method with Blöch corrections and Gaussian smearing method, respectively. The structural relaxation was performed using the conjugate gradient method until total energy is converged to within  $10^{-5}$  eV and the force on each atom is less than  $0.01 \text{ eV} \cdot \text{\AA}^{-1}$ . The phonon spectra of the *Cmmm* structure was calculated by the finite displacement method, which is based on first-principles calculations of total energy, Hellman-Feynman forces, and the dynamical matrix as implemented in the PHONOPY

package [29]. The independent single crystal elastic constants were determined from evaluation of stress tensor generated small strain (stress-strain approach) [30], and the polycrystalline elastic moduli including bulk modulus, shear modulus and Young's modulus, as well as Poisson's ratio, were thus estimated by the Voigt-Reuss-Hill approximation [31].

### 3. Results and Discussion

Under ambient conditions, the structure searches with the only input being the chemical composition of Ir:Zr = 2:1 predicted the most stable structure to be the orthorhombic  $Cmmm$  structure containing four f.u. per unit cell, as presented in Figure 1b, together with the previous experimental  $Cu_2Mg$ -type phase Figure 1a. Compared to the building block ( $ZrIr_{10}$ ) in the  $Cu_2Mg$ -type phase, each Zr atom is surrounded by twelve Ir atoms in the  $Cmmm$  structure, resulting in a different polyhedron building block. By the full relaxations of both lattice constants and internal atomic coordinations, the equilibrium structural parameters of  $Cmmm$  structure are calculated to be  $a = 12.477 \text{ \AA}$ ,  $b = 4.012 \text{ \AA}$ , and  $c = 3.946 \text{ \AA}$ , with four inequivalent atoms Zr, Ir1, Ir2, and Ir3 occupying  $4g (0.653, 0, 0)$ ,  $2a (0, 0, 0)$ ,  $2c (0.5, 0, 0.5)$ , and  $4g (0.836, 0, 0.5)$  positions, respectively. Figure 1c presents the dependence of the total energy on the f.u. volume for  $Cmmm$  and  $Cu_2Mg$ -type phases; it can be clearly seen that, for  $Ir_2Zr$ , the predicted  $Cmmm$  structure is energetically far more stable than  $Cu_2Mg$ -type structure, and this further confirms our structural prediction. Moreover, by fitting the third-order Birch-Murnaghan equation of state (EOS) [32] based on the calculated  $E-V$  data (Figure 1c), the zero-pressure bulk modulus ( $B_0$ ) and its pressure derivatives ( $B_0'$ ) of  $Cmmm$  phase is determined to be 235 GPa and 4.691, respectively. The dynamical stability of a crystalline structure requires the eigen frequencies of its lattice vibrations be real for all wave vectors in the whole Brillouin zone. As shown in Figure 1d, no imaginary phonon frequency was detected in the whole Brillouin zone for the predicted  $Cmmm$  phase, indicating its dynamical stability at ambient pressure.

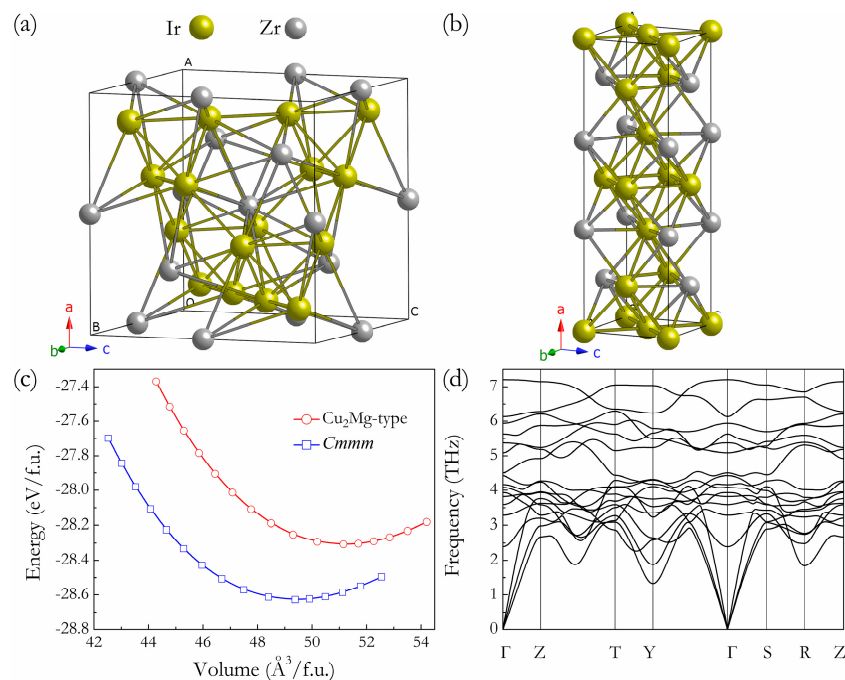


**Figure 1.** Crystal structures of  $Cu_2Mg$ - $Ir_2Zr$  (a) and  $Cmmm$ - $Ir_2Zr$  (b), the large and small spheres represent Ir and Zr atoms, respectively. The total energy vs. f.u. volume for  $Cu_2Mg$ -type and  $Cmmm$  structures (c) and phonon dispersion curves of  $Cmmm$ - $Ir_2Zr$  at 0 GPa (d).

The formation enthalpy vs. composition plot, called a convex hull, is the set of lines connecting the lowest energy structures, and any structure whose formation enthalpy lies on the convex hull

is deemed stable and synthesizable in principle [33]. In the Ir-Zr system, the formation enthalpy of each  $\text{Ir}_x\text{Zr}_y$  intermetallic with respect to the *fcc*-Ir and  $\alpha$ -Zr separate phases is quantified by the formula. Based on the calculated formation enthalpy for each  $\text{Ir}_x\text{Zr}_y$  intermetallic compound, we reconstructed the convex hull line for the Ir-Zr system, as shown in Figure 2. One can see that the formation enthalpy of Ir-Zr intermetallic decreases when  $x < 0.5$ , while the formation enthalpy increases when  $x > 0.5$ . The *Cmcm*-IrZr is the most stable intermetallic compound among all the studied intermetallic compounds, which is in excellent agreement with the previous works [18]. The predicted *Cmmm* structure for  $\text{Ir}_2\text{Zr}$  matches evidently with the convex hull curve between the experimental  $\text{L1}_2$ - $\text{Ir}_3\text{Zr}$  and *Cmcm*-IrZr phases, indicating the possible synthesis of this composition in the real experiment. However, the previously proposed  $\text{Cu}_2\text{Mg}$ -type phase for  $\text{Ir}_2\text{Zr}$  is located above the convex hull line and possesses a higher formation enthalpy, at 107 meV/atom, than that of the *Cmmm* phase, suggesting that the  $\text{Cu}_2\text{Mg}$ -type phase for  $\text{Ir}_2\text{Zr}$  is indeed metastable. In addition, we suppose that the synthetic conditions of *Cmmm*- $\text{Ir}_2\text{Zr}$  may be similar to those observed for the formation of  $\text{Ir}_3\text{Zr}_5$  for their similar values for formation enthalpies presented in the convex hull line.

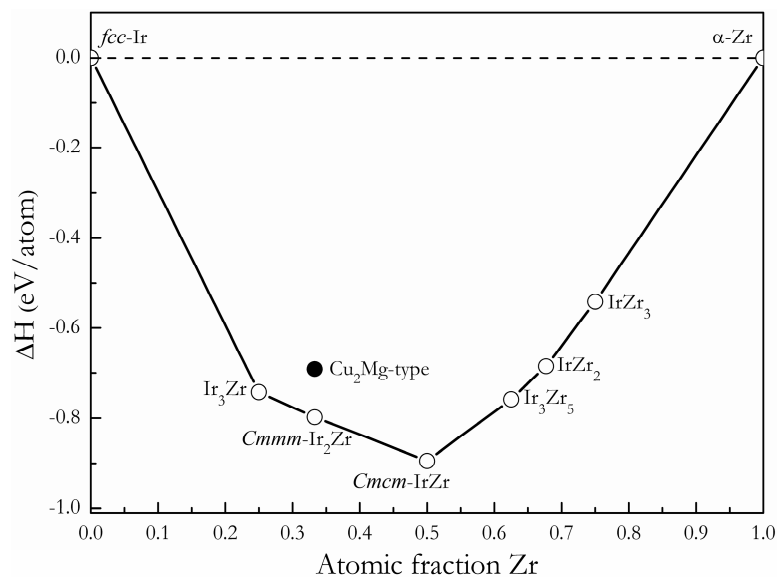


**Figure 2.** The formation enthalpy vs. composition curves for stoichiometric intermetallics in Ir-Zr system with *fcc*-Ir and  $\alpha$ -Zr as reference states. The solid line denotes the ground state convex hull.

As a new intermetallic phase in the Ir-Zr system, the mechanical properties of *Cmmm*- $\text{Ir}_2\text{Zr}$  are important for high-temperature applications. Tables 1 and 2 present the calculated results on the mechanical parameters of *Cmmm*- $\text{Ir}_2\text{Zr}$  and  $\text{Cu}_2\text{Mg}$ - $\text{Ir}_2\text{Zr}$ , including the single crystal elastic constants ( $C_{ij}$ ), polycrystalline elastic modulus, and hardness, which are determined from the calculated  $C_{ij}$  by applying a set of given strains. Under the stress-strain approach [30], for a given set of strains  $\boldsymbol{\varepsilon} = (\varepsilon_1, \varepsilon_2, \varepsilon_3, \varepsilon_4, \varepsilon_5, \varepsilon_6)$  (where  $\varepsilon_1, \varepsilon_2,$  and  $\varepsilon_3$  are the normal strains and others are the shear strains) imposed on a crystal, correspondingly, one set of stresses  $\boldsymbol{\sigma} = (\sigma_1, \sigma_2, \sigma_3, \sigma_4, \sigma_5, \sigma_6)$  can be determined on the deformed lattice in terms of first-principles calculations; herein, the elastic stiffness constant matrix  $\mathbf{C}$  links  $\boldsymbol{\varepsilon}$  and  $\boldsymbol{\sigma}$  by  $\boldsymbol{\sigma} = \boldsymbol{\varepsilon} \mathbf{C}$ . Based on the obtained elastic constants, bulk modulus  $B$  and shear modulus  $G$  are evaluated by using the Voigt-Reuss-Hill approximation [31], and the Young's modulus  $E$  and Poisson's ratio  $\nu$  are derived from the equations of  $E = 9BG = (3B + G)$  and  $\nu = (3B - 2G) / (6B + 2G)$ , respectively. The empirical model of  $H_v = 2(k^2G)^{0.585} - 3$  ( $k = G/B$ ) proposed by Chen et al. [34] employed here to estimate the hardness of  $\text{Ir}_2\text{Zr}$ . As listed in Table 1, the three independent  $C_{ij}$  calculated for the cubic  $\text{Cu}_2\text{Mg}$ - $\text{Ir}_2\text{Zr}$  are in excellent agreement with the previous theoretical results [18], confirming the reliability of the present results and the accuracy of the elastic constant calculations. The mechanical stability of the predicted *Cmmm* phase satisfies the Born-Huang criterion for an orthorhombic crystal [35]:

( $C_{11} > 0, C_{44} > 0, C_{55} > 0, C_{66} > 0, C_{11}C_{22} > C_{12}^2, C_{11}C_{22}C_{33} + 2C_{12}C_{13}C_{23} - C_{11}C_{23}^2 - C_{22}C_{13}^2 - C_{33}C_{12}^2 > 0$ ), thus suggesting that the *Cmmm* phase is mechanically stable under ambient conditions. In addition, the calculated results for the *Cmmm* phase showed that the  $C_{ij}$  possess the trend  $C_{11} \approx C_{22} \approx C_{33}$ , suggesting that it is nearly the same uniaxial compression resistance along the three main crystal directions. Polycrystalline elastic modulus, another important parameter, also contains information regarding the hardness of a material with respect to various types of deformation. Bulk modulus  $B$  measures the resistance of a material to volume change and provides an estimate of its response to a hydrostatic pressure, shear modulus  $G$  describes the resistance of a material to shape change, and Young's modulus  $E$  measures the resistance against uniaxial tension. From Table 2, firstly, it should be noted that the derived Hill bulk modulus  $B$  of *Cmmm* phase (239 GPa) agrees well with that obtained directly from the fitting of the Birch-Murnaghan EOS ( $B_0 = 235$  GPa), which further demonstrates the accuracy of our elastic constant calculations. Secondly, the calculated values of bulk modulus  $B$ , shear modulus  $G$ , Young's modulus  $E$ , and hardness for *Cmmm* phase are close to those of  $\text{Cu}_2\text{Mg}$ -type phase, indicating their similar polycrystalline mechanical behaviors. Thirdly, according to the Pugh criterion [36], the intrinsically brittle nature of both *Cmmm* and  $\text{Cu}_2\text{Mg}$ -type structures for  $\text{Ir}_2\text{Zr}$  can be revealed by its  $B/G$  ratio of 2.038 and 1.920, which is larger than the critical value of 1.75.

**Table 1.** Calculated single elastic constants  $C_{ij}$  (in GPa) of  $\text{Cu}_2\text{Mg}$ -type and *Cmmm* phases for  $\text{Ir}_2\text{Zr}$  intermetallic compound.

$\text{Ir}_2\text{Zr}$	Source	$C_{11}$	$C_{22}$	$C_{33}$	$C_{44}$	$C_{55}$	$C_{66}$	$C_{12}$	$C_{13}$	$C_{23}$
$\text{Cu}_2\text{Mg}$ -type	This work	379	-	-	152	-	-	181	-	-
-	Theory [18]	379	-	-	151	-	-	180	-	-
<i>Cmmm</i>	This work	362	348	378	97	162	164	173	188	174

**Table 2.** Calculated polycrystalline bulk modulus  $B$ , shear modulus  $G$ , Young's modulus  $E$ , and hardness  $H$  (in units of GPa) for  $\text{Ir}_2\text{Zr}$ . Also shown are Poisson's ratio  $\nu$  and  $B/G$  ratio.

$\text{Ir}_2\text{Zr}$	Source	$B$	$G$	$E$	$\nu$	$B/G$	$H$
$\text{Cu}_2\text{Mg}$ -type	This work	248	129	323	0.283	1.972	18.9
-	Theory [18]	246	128	327	0.278	1.920	20.3
<i>Cmmm</i>	This work	239	117	302	0.289	2.038	18.4

The elastic anisotropic property, which is strongly related to the mechanical strength of solid materials, has important implications in engineering applications, such as microcracks, anisotropic plastic deformation, elastic durability, etc. Compared to the reported results of other known intermetallic compounds in the Ir-Zr system, the studies on the elastic anisotropic behaviors of this new *Cmmm* phase are of great importance for its technical applications in high-temperature environments. As outlined by Panda et al. [37] and He et al. [38], executing the appropriate coordinate system transformations for the compliances allows the determination of the variation of bulk modulus  $B$ , Young's moduli  $E$ , and shear modulus  $G$  with crystallographic direction,  $[uvw]$ , for a given crystallographic plane,  $(hkl)$ , containing these directions, (i.e.,  $B_{[uvw]}$ ,  $E_{[uvw]}$ , and  $G_{(hkl)[uvw]}$ ). For orthorhombic *Cmmm* phase, the bulk modulus  $B$  and Young's modulus  $E$  can be expressed as:

$$B^{-1} = (s_{11} + s_{12} + s_{13})\alpha^2 + (s_{12} + s_{22} + s_{23})\beta^2 + (s_{13} + s_{23} + s_{33})\gamma^2 \quad (1)$$

$$E^{-1} = s_{11}\alpha^4 + s_{22}\beta^4 + s_{33}\gamma^4 + 2s_{12}\alpha^2\beta^2 + 2s_{23}\beta^2\gamma^2 + 2s_{13}\alpha^2\gamma^2 + s_{44}\beta^2\gamma^2 + s_{55}\alpha^2\gamma^2 + s_{66}\alpha^2\beta^2 \quad (2)$$

where  $\alpha$ ,  $\beta$ , and  $\gamma$  are the direction cosines of  $[uvw]$  direction, and  $s_{11}$ ,  $s_{22}$ , etc. are the elastic compliance constants given by Ney [39]. The shear modulus  $G$  on the  $(hkl)$  shear plane with shear stress applied along  $[uvw]$  direction is given by:

$$G^{-1} = 4s_{11}\alpha_1^2\alpha_2^2 + 4s_{22}\beta_1^2\beta_2^2 + 4s_{33}\gamma_1^2\gamma_2^2 + 8s_{12}\alpha_1\alpha_2\beta_1\beta_2 + 8s_{23}\beta_1\beta_2\gamma_1\gamma_2 + 8s_{13}\alpha_1\alpha_2\gamma_1\gamma_2 + s_{44}(\beta_1\gamma_2 + \beta_2\gamma_1)^2 + s_{55}(\alpha_1\gamma_2 + \alpha_2\gamma_1)^2 + s_{66}(\alpha_1\beta_2 + \alpha_2\beta_1)^2 \quad (3)$$

where  $\alpha_1$ ,  $\beta_1$ ,  $\gamma_1$ ,  $\alpha_2$ ,  $\beta_2$ ,  $\gamma_2$  are the direction cosines of the  $[uvw]$  and  $[HKL]$  directions in the coordinate systems, where the  $[HKL]$  denotes the vector normal to the  $(hkl)$  shear plane. The three-dimensional (3D) surface representations showing the variation of the bulk modulus  $B$  and Young's modulus  $E$  are plotted in Figure 3a,c, and the distance from the origin of the system of coordinates to this surface is equal to the  $B$  or  $E$  in a given direction. The plane projections ( $ab$ ,  $ac$ , and  $bc$  planes) of the directional dependences of the bulk modulus  $B$  and Young's modulus  $E$  are given in Figure 3b,d for comparison. It can be seen that  $Cmmm$ -Ir<sub>2</sub>Zr exhibits a highly pronounced elastic anisotropy, as its 3D picture shows a large deviation from the spherical shape, which qualifies an isotropic medium. From Figure 3b,d, the distributions of bulk modulus  $B$  and Young's modulus  $E$  within the crystal plane  $bc$  display the largest and the smallest elastic anisotropy behaviors, respectively. In more detail, the changes of Young's moduli along different crystal directions within four specific planes (001), (100), (010), and (1 $\bar{1}$ 0) are presented in Figure 4a. For example, the variation of Young's modulus  $E$  in the (100) plane for the quadrant of directions  $[uvw]$  between [001] ( $\theta = 0^\circ$ ) and [010] ( $\theta = 90^\circ$ ), the  $Cmmm$  phase displays the smallest elastic anisotropy behavior (as shown in Figure 3d) with a maximum of 254 GPa and a minimum of 240 GPa. The selected directional Young's moduli along the five principal crystallographic directions are denoted as in Figure 4a, and it can be seen that the calculated values for  $E$  decrease in the following order:  $E_{[100]} \approx E_{[010]} < E_{[011]} < E_{[001]} < E_{[110]} < E_{[110]} < E_{[101]} < E_{[1\bar{1}0]} < E_{[1\bar{1}1]}$ . Similarly, Figure 4b presents the orientation dependence of the shear modulus along arbitrary shear directions within these four shear planes. Compared to the other three shear planes, the calculations show that the shear modulus for a shear deformation within the (100) plane is not only nearly isotropic [ $G_{max} = G_{[010]} = 164$  GPa and  $G_{min} = G_{[001]} = 162$  GPa] but also has greater resistance to shear deformations.

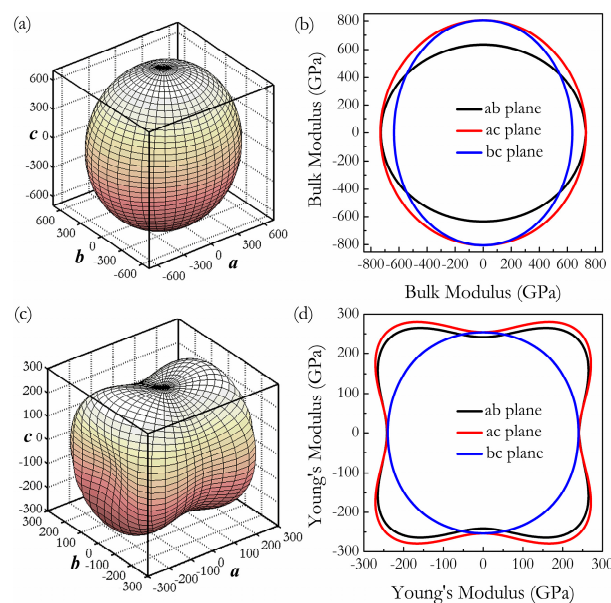


**Figure 3.** Three-dimensional surface representations of bulk modulus  $B$  (a) and the Young's modulus  $E$  (b) at 0 GPa, and the projections of bulk modulus  $B$  (c) and the Young's modulus  $E$  (d) within  $ab$ ,  $ac$ , and  $bc$  planes.

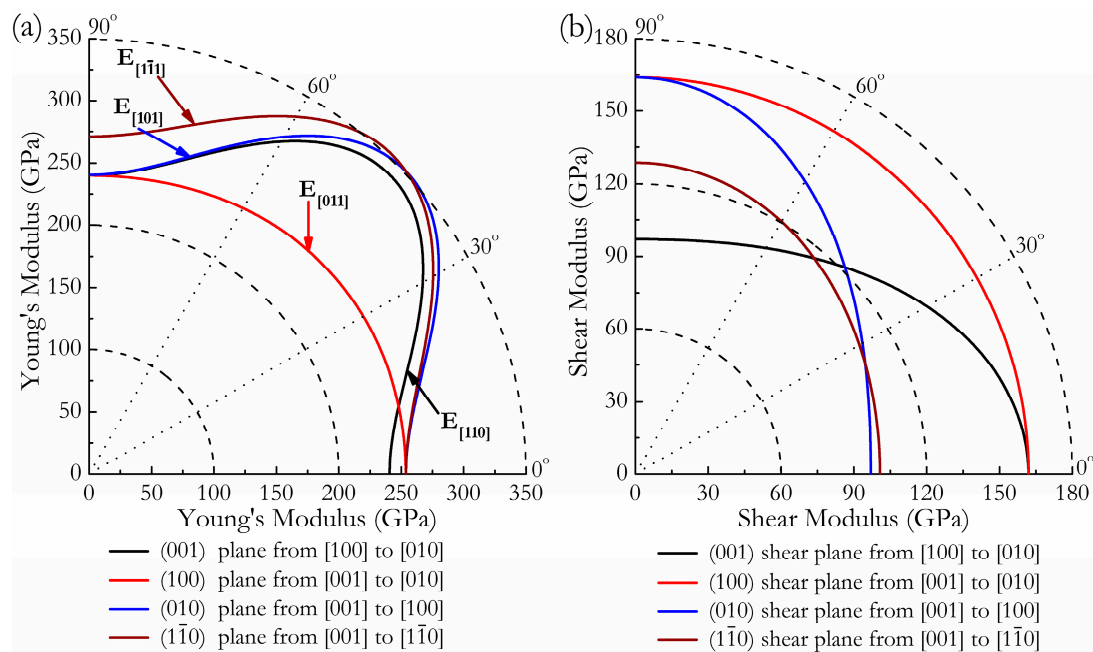


**Figure 4.** Orientation dependences of the Young's modulus  $E$  (a) and shear modulus  $G$  (b) for  $Cmmm$ - $Ir_2Zr$ .

To understand the bonding mechanism of intermetallic  $Ir_2Zr$  on a fundamental level, the total and partial density of state ( $t$ -DOS and  $p$ -DOS) of  $Cu_2Mg$ -type and  $Cmmm$  phases at ambient pressure are calculated and presented in Figure 5, where the vertical dashed line is the Fermi level ( $E_F$ ). It is clear that both structures are metal for the finite values of  $t$ -DOS at the  $E_F$ . The typical feature of the  $t$ -DOS for these two compounds is the presence of so-called "pseudogap" (a sharp valley around the  $E_F$ ), a borderline between the bonding and antibonding orbital [40]. It has been suggested that the location of  $E_F$  in the DOS profiles can reflect the structural stability of the compounds. For the  $Cu_2Mg$ -type phase, the  $E_F$  lies to the right of the pseudogap (i.e., within the antibonding states), suggesting their metastable nature, while for  $Cmmm$  phase, the  $E_F$  locates at the left of the pseudogap (i.e., within the bonding states) with relative lower electronic density of state  $N(E_F)$  values, revealing its structural stability. These findings support the previous results acquired from the formation enthalpy calculations. The feature of  $p$ -DOSs for both phases indicates that there is strong interaction between Ir and Zr atoms through  $d$ - $d$  hybridization, which can be seen from the hybridization peaks of Ir- $d$  and Zr- $d$  orbitals plotted in Figure 5a,b, signifying the existence of directional covalent-like bonding in  $Ir_2Zr$  intermetallic compound. A careful comparison further reveals that the  $p$ -DOS of the Ir and Zr atoms in  $Cmmm$ - $Ir_2Zr$  are more localized than those in  $Cu_2Mg$ - $Ir_2Zr$ , resulting a small bandwidth of  $p$ -DOS and a lower  $N(E_F)$ . It is known that for the most stable structure, there is enough room to accommodate all its valence electrons into bonding states, so as to bring the  $E_F$  to a valley position separating bonding and antibonding states (pseudogap) favorable for structural stability. Therefore, the formation of  $Cmmm$  intermetallic phase is energetically more favorable than the previously proposed  $Cu_2Mg$ -type for  $Ir_2Zr$ .

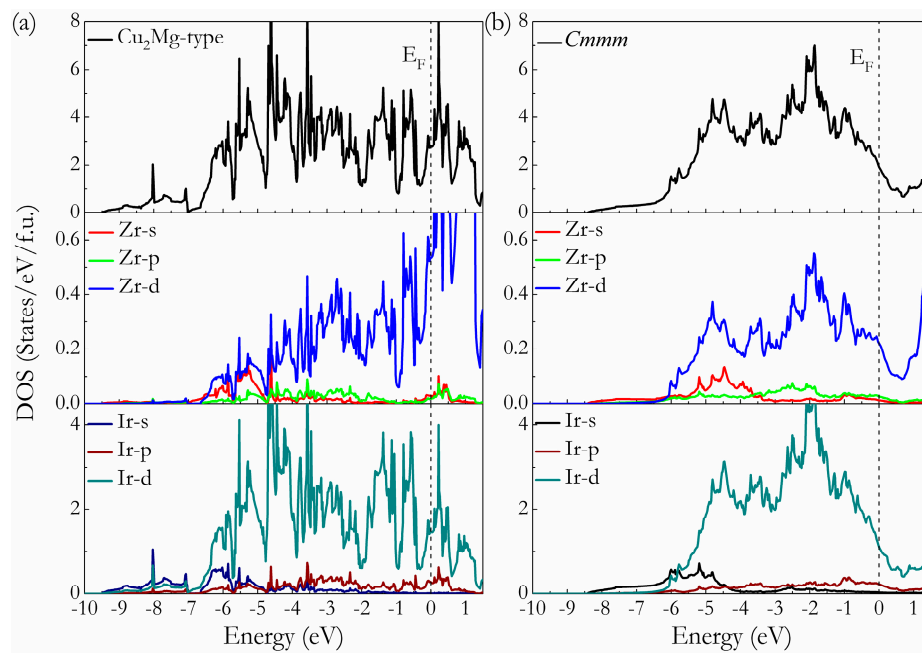


**Figure 5.** Calculated total and partial DOS of Cu<sub>2</sub>Mg-Ir<sub>2</sub>Zr (a) and Cmmm-Ir<sub>2</sub>Zr (b). The vertical dash line is the  $E_F$ .

#### 4. Conclusions

In summary, we have extensively explored the ground-state structures of stoichiometric Ir<sub>2</sub>Zr intermetallic compound by using the recently developed particle swarm optimization algorithm in crystal structure prediction. A new orthorhombic Cmmm structure was proposed as the best candidate at ground state that is energetically more favorable than the previous experimental Cu<sub>2</sub>Mg-type structure, as demonstrated by the total energy and formation enthalpy calculations. Then, the mechanical and electronic properties of this new predicted Cmmm phase were fully investigated in comparisons with Cu<sub>2</sub>Mg-type phase. The predicted Cmmm phase exhibits nearly elastic isotropic behavior and great resistance to shear deformations within (100) crystal plane according to the directional elastic moduli calculations. Evidence of atomic bonding related to the structural stability for Ir<sub>2</sub>Zr was obtained by calculation of the electronic structures.

**Acknowledgments:** This work was supported by the National Undergraduate Innovative Training Program (No. 201610721004), the Natural Science New Star of Science and Technologies Research Plan in Shaanxi Province of China (Grant No. 2017KJXX-53), the Natural Science Basic Research plan in Shaanxi Province of China (Grant No. 2016JM1016), and the Baoji University of Arts and Sciences Key Research (Grant No. ZK16068). The all authors thank the computing facilities at High Performance Computing Center of Baoji University of Arts and Sciences.

**Author Contributions:** Meiguang Zhang and Ke Cheng conceived and designed the projects; Meiguang Zhang, Rui Cao, Meijie Zhao and Juan Du performed the calculations; Meiguang Zhang Rui Cao, Meijie Du and Juan Du prepared the manuscript; Ke Cheng revised the paper; all authors discussed the results and commented on the manuscript.

**Conflicts of Interest:** The authors declare no conflict of interest.

#### References

1. Kuznetsova, T.; Zubar, T.; Chizhik, S.; Gilewicz, A.; Lupicka, O.; Warcholinski, B. Surface microstructure of Mo(C)N coatings investigated by AFM. *J. Mater. Eng. Perform.* **2016**, *25*, 5450–5459. [[CrossRef](#)]
2. Warcholinski, B.; Gilewicz, A.; Lupicka, O.; Kuprin, A.S.; Tolmachova, G.N.; Ovcharenko, V.D.; Kolodiy, I.V.; Sawczak, M.; Kochmanska, A.E.; Kochmanski, P.; et al. Structure of CrON coatings formed in vacuum arc plasma fluxes. *Surf. Coat. Technol.* **2017**, *309*, 920–930. [[CrossRef](#)]

3. Warcholinski, B.; Gilewicz, A.; Kuznetsova, T.A.; Zubar, T.I.; Chizhik, S.A.; Abetkovskaia, S.O.; Lapitskaya, V.A. Mechanical properties of Mo(C)N coatings deposited using cathodic arc evaporation. *Surf. Coat. Technol.* **2017**, *319*, 117–128. [[CrossRef](#)]
4. Yamabe-Mitarai, Y.; Ro, Y.; Maruko, T.; Harada, H. Microstructure dependence of strength of Ir-base refractory superalloys. *Intermetallics* **1999**, *7*, 49–58. [[CrossRef](#)]
5. Ran, H.T.; Du, Z.M. Thermodynamic assessment of the Ir-Zr system. *J. Alloys Compd.* **2006**, *413*, 101–105. [[CrossRef](#)]
6. Sha, J.B.; Yamabe-Mitarai, Y.; Harada, H. Microstructural evaluation and mechanical properties of Ir-Hf-Zr ternary alloys at room and high temperatures. *Intermetallics* **2006**, *14*, 1364–1369. [[CrossRef](#)]
7. Yamabe-Mitarai, Y.; Gu, Y.; Harada, H.; Huang, C. Compressive creep properties of Ir-base refractory superalloys. *Metall. Mater. Trans. A* **2005**, *36*, 547–557. [[CrossRef](#)]
8. Yamabe-Mitarai, Y.; Harada, H. Face centered cubic and L<sub>12</sub> two-phase structure of Ir-Nb-Zr alloys. *J. Alloys Compd.* **2003**, *361*, 169–179. [[CrossRef](#)]
9. Kim, W.Y.; Tanaka, H.; Kasama, A.; Hanada, S. Microstructure and room temperature fracture toughness of Nb<sub>ss</sub>/Nb<sub>5</sub>Si<sub>3</sub> in situ composites. *Intermetallics* **2001**, *9*, 827–834. [[CrossRef](#)]
10. Chen, B.S.; Li, Y.Z.; Guan, X.Y.; Wang, C.; Wang, C.X.; Gao, Z.Y. First-principles study of structural, elastic and electronic properties of ZrIr alloy. *Comput. Mater. Sci.* **2015**, *105*, 66–70. [[CrossRef](#)]
11. Kudryavtsev, Y.V.; Semenova, O.L. Shape memory effect in ZrIr and Zr-Ir-Co alloys. *Powder Metall. Met. Ceram.* **2011**, *50*, 471–478. [[CrossRef](#)]
12. Okamoto, H. The Ir-Zr (iridium-zirconium) system. *J. Phase Equilib.* **1992**, *13*, 653–656. [[CrossRef](#)]
13. Eremenko, V.N.; Semenova, E.L.; Shtepa, T.D. State diagram of the Zr-Ir system. *Russ. Metall.* **1980**, *5*, 210–213.
14. Semenova, E.L.; Kudryavtsev, Y.V. Structural phase transformation and shape memory effect in ZrRh and ZrIr. *J. Alloys Compd.* **1994**, *203*, 165–168. [[CrossRef](#)]
15. Stalick, J.K.; Waterstrat, R.M. The crystal structure of martensitic ZrIr and ZrRh. *J. Alloys Compd.* **2009**, *477*, 123–126. [[CrossRef](#)]
16. Xing, W.; Chen, X.Q.; Li, D.Z.; Li, Y.Y.; Fu, C.L.; Meschel, S.V.; Ding, X. First-principles studies of structural stabilities and enthalpies of formation of refractory intermetallics: TM and TM<sub>3</sub> (T = Ti, Zr, Hf; M = Ru, Rh, Pd, Os, Ir, Pt). *Intermetallics* **2012**, *28*, 16–24. [[CrossRef](#)]
17. Hart, G.L.; Curtarolo, S.; Massalski, T.B.; Levy, O. Comprehensive search for new phases and compounds in binary alloy systems based on platinum-group metals, using a computational first-principles approach. *Phys. Rev. X* **2013**, *3*, 041035. [[CrossRef](#)]
18. Wu, J.; Zhang, B.; Zhan, Y. *Ab initio* investigation into the structure and properties of Ir-Zr intermetallics for high-temperature structural applications. *Comput. Mater. Sci.* **2017**, *131*, 146–159. [[CrossRef](#)]
19. Wang, Y.C.; Lv, J.; Zhu, L.; Ma, Y.M. Crystal structure prediction via particle swarm optimization. *Phys. Rev. B* **2010**, *82*, 094116. [[CrossRef](#)]
20. Wang, Y.C.; Lv, J.; Zhu, L.; Ma, Y.M. CALYPSO: A method for crystal structure prediction. *Comput. Phys. Commun.* **2012**, *183*, 2063–2070. [[CrossRef](#)]
21. Lv, J.; Wang, Y.C.; Zhu, L.; Ma, Y.M. Predicted novel high-pressure phases of lithium. *Phys. Rev. Lett.* **2011**, *106*, 015503. [[CrossRef](#)] [[PubMed](#)]
22. Zhu, L.; Wang, H.; Wang, Y.C.; Lv, J.; Ma, Y.M.; Cui, Q.L.; Ma, Y.M.; Zou, G.T. Substitutionally alloy of Bi and Te at high pressure. *Phys. Rev. Lett.* **2011**, *106*, 145501. [[CrossRef](#)] [[PubMed](#)]
23. Li, Y.W.; Hao, J.; Liu, H.Y.; Li, Y.L.; Ma, Y.M. The metallization and superconductivity of dense hydrogen sulfide. *J. Chem. Phys.* **2014**, *140*, 174712. [[CrossRef](#)] [[PubMed](#)]
24. Kresse, G.; Furthmüller, J. Efficiency of ab-initio total energy calculations for metals and semiconductors using a plane-wave basis set. *Comput. Mater. Sci.* **1996**, *6*, 15–50. [[CrossRef](#)]
25. Perdew, J.P.; Burke, K.; Ernzerhof, M. Generalized gradient approximation made simple. *Phys. Rev. Lett.* **1996**, *77*, 3865. [[CrossRef](#)] [[PubMed](#)]
26. Perdew, J.P.; Chevary, J.A.; Vosko, S.H.; Jackson, K.A.; Pederson, M.R.; Singh, D.J.; Fiolhais, C. Atoms, molecules, solids, and surfaces: Applications of the generalized gradient approximation for exchange and correlation. *Phys. Rev. B* **1992**, *46*, 6671. [[CrossRef](#)]
27. Kresse, G.; Joubert, D. From ultrasoft pseudopotentials to the projector augmented-wave method. *Phys. Rev. B* **1999**, *59*, 1758. [[CrossRef](#)]
28. Monkhorst, H.J.; Pack, J.D. Special points for Brillouin-zone integrations. *Phys. Rev. B* **1976**, *13*, 5188. [[CrossRef](#)]

29. Togo, A.; Oba, F.; Tanaka, I. First-principles calculations of the ferroelastic transition between rutile-type and  $\text{CaCl}_2$ -type  $\text{SiO}_2$  at high pressures. *Phys. Rev. B* **2008**, *78*, 134106. [[CrossRef](#)]
30. Milman, V.; Warren, M.C. Elasticity of hexagonal BeO. *J. Phys. Condens. Matter* **2001**, *13*, 241. [[CrossRef](#)]
31. Hill, R. The elastic behaviour of a crystalline aggregate. *Proc. Phys. Soc. Sect. A* **1952**, *65*, 349. [[CrossRef](#)]
32. Birch, F. Finite elastic strain of cubic crystals. *Phys. Rev.* **1947**, *71*, 809. [[CrossRef](#)]
33. Ghosh, G.; Van de Walle, A.; Asta, M. First-principles calculations of the structural and thermodynamic properties of bcc, fcc and hcp solid solutions in the Al-TM (TM = Ti, Zr and Hf) systems: A comparison of cluster expansion and supercell methods. *Acta Mater.* **2008**, *56*, 3202–3221. [[CrossRef](#)]
34. Chen, X.Q.; Niu, H.Y.; Li, D.Z.; Li, Y.Y. Modeling hardness of polycrystalline materials and bulk metallic glasses. *Intermetallics* **2011**, *19*, 1275–1281. [[CrossRef](#)]
35. Born, M. On the stability of crystal lattices. *Math. Proc. Camb. Philos. Soc.* **1940**, *36*, 160–172. [[CrossRef](#)]
36. Pugh, S.F. XCII. Relations between the elastic moduli and the plastic properties of polycrystalline pure metals. *Philos. Mag.* **1954**, *45*, 823–843. [[CrossRef](#)]
37. Panda, K.B.; Ravi Chandran, K.S. Determination of elastic constants of titanium diboride ( $\text{TiB}_2$ ) from first principles using FLAPW implementation of the density functional theory. *Comput. Mater. Sci.* **2006**, *35*, 134–150. [[CrossRef](#)]
38. He, Y.; Schwarz, R.B.; Migliori, A. Elastic constants of single crystal  $\gamma$ -TiAl. *J. Mater. Res.* **1995**, *10*, 1187–1195. [[CrossRef](#)]
39. Nye, J.F. *Physical Properties of Crystals: Their Representation by Tensors and Matrices*; Oxford University Press: Oxford, UK, 1985.
40. Vajeeston, P.; Ravindran, P.; Ravi, C.; Asokamani, R. Electronic structure, bonding, and ground-state properties of  $\text{AlB}_2$ -type transition-metal diborides. *Phys. Rev. B* **2001**, *63*, 045115. [[CrossRef](#)]



© 2018 by the authors. Licensee MDPI, Basel, Switzerland. This article is an open access article distributed under the terms and conditions of the Creative Commons Attribution (CC BY) license (<http://creativecommons.org/licenses/by/4.0/>).